

# Solar Photoelectroreduction of Nitrate Ions on $\text{PbI}_2/\text{CuI}$ Nanocomposite Electrodes

Egon Kecsenovity, Saji Thomas Kochuveedu, Jyh-Pin Chou, Diána Lukács, Ádám Gali, and Csaba Janáky\*

Solar light-driven photoelectrochemical conversion of nitrate ions to nitrite is achieved on copper-lead iodide nanocomposite electrodes. By optimizing the composition,  $1.2 \pm 0.05 \text{ mA cm}^{-2}$  photocurrent density is obtained under concentrated solar irradiation. The reduction products are  $\text{NO}_2^-$  and  $\text{N}_2$ , at 0.61 V reversible hydrogen electrode (RHE), which is at least 600 mV higher than the redox potential of these processes. The faradaic efficiency of  $\text{NO}_2^-$  ion formation is up to 52% while no hydrogen evolution occurs. Optical studies show the possibility of exciting electrons from the valence band of CuI to the conduction band of  $\text{PbI}_2$  upon illumination, extending the visible light absorption of the nanocomposite photoelectrode. Experimental and theoretical optoelectronic studies indicate that CuI and  $\text{PbI}_2$  are held together by weak attractive forces (also excluding the formation of a new compound), which opens a new strategy to design metal halide nanocomposite photoelectrodes with tailored properties.

removal of organic and inorganic contaminants from water, and biosensing are a few among them. Reduction of nitrate ions is a specifically interesting area because the high content of nitrate ions in fertilizers easily contaminates surface and groundwater.

The existing methods for nitrate removal are ion exchange, reverse osmosis, and electro dialysis, but these processes have limitation due to their expensive operation and subsequent disposal problem of the generated nitrate waste brine. Chemical-based dinitration includes a few steps, where reduction of nitrate to nitrite is considered as the rate-determining step of the whole process. Nitrite ions are further reduced to  $\text{N}_2$ , and/or ammonia depending on the selectivity of the catalyst. Promoting the rate-determining step can lead to the

## 1. Introduction

Photoelectrochemistry is a lucrative approach to utilize the abundant solar energy to produce fuels and basic chemicals with a small carbon footprint. While generation of hydrogen from water and conversion of carbon dioxide still dominate the field, there are other avenues to explore.<sup>[1]</sup> Disinfection of water and air,


alternate ways of nitrate reduction.<sup>[2,3]</sup> Although photocatalysis and electrocatalysis have been already applied in this area, these two approaches have their own limitations. Electrolysis often demands large bias voltage and noble metals, whereas semiconductor-based photocatalysis suffers from setbacks such as narrow absorption spectra, low quantum efficiency, and recombination of charge carriers. Photoelectrochemistry receives great attention because it can combine advantages of photocatalysis and electrolysis, and therefore can reduce or oxidize pollutants, such as nitrate ions in drinking water. However, many hurdles must be overcome to realize the full potential of a photoelectrochemical (PEC) cell. A few among them are exploiting the maximum solar spectrum, and developing efficient and reliable semiconductor photoelectrode materials.

There are only a few reports on PEC nitrate reduction, based on p-GaInP<sub>2</sub><sup>[4]</sup> and Si.<sup>[3]</sup> p-GaInP<sub>2</sub> photoelectrode exhibited high PEC activity ( $10 \text{ mA cm}^{-2}$ ) and high faradaic efficiency [FE] of 80%) in converting nitrate to nitrite. p-GaInP<sub>2</sub> electrodes, however, are of high cost and require complicated fabrication process. Low-cost Si photoelectrode also generated high current density ( $17 \text{ mA cm}^{-2}$ ) and showed 65% FE in nitrate reduction, although with limited stability. Furthermore, our survey on recent reports (Table S1, Supporting Information) shows that in photochemical, electrochemical, and PEC nitrate reduction, the parasitic hydrogen evolution reaction (HER) is an issue to be solved in most of the cases.<sup>[5,6]</sup> Therefore, one major objective of this work was to establish a reliable method for the selective reduction of nitrate to nitrite under ambient condition while avoiding the HER.

E. Kecsenovity, Dr. S. T. Kochuveedu, Prof. C. Janáky  
Department of Physical Chemistry and Materials Science  
Interdisciplinary Excellence Centre  
University of Szeged  
Rerrich Square 1, Szeged H-6720, Hungary  
E-mail: janaky@chem.u-szeged.hu

Dr. J.-P. Chou, Prof. Á. Gali  
Institute for Solid State Physics and Optics  
Wigner Research Centre for Physics  
Konkoly-Thege Miklós út 29-33, Budapest H-1121, Hungary

D. Lukács  
Department of Analytical Chemistry  
University of Pannonia  
Egyetem u. 10, Veszprém 8200, Hungary

 The ORCID identification number(s) for the author(s) of this article can be found under <https://doi.org/10.1002/solr.202000418>.

© 2020 The Authors. Published by Wiley-VCH GmbH. This is an open access article under the terms of the Creative Commons Attribution-NonCommercial-NoDerivs License, which permits use and distribution in any medium, provided the original work is properly cited, the use is non-commercial and no modifications or adaptations are made.

DOI: 10.1002/solr.202000418

Metal halide semiconductors are considered as new class of materials with favorable combination of optical and electronic properties, and with the ease to be solution processed into films.<sup>[7,8]</sup> These semiconductors received particularly great attention in metal halide perovskite-based solar energy conversion devices.<sup>[9–13]</sup> Among the metal halides, lead iodide (PbI<sub>2</sub>) occupies a creditable place owing to its narrow direct bandgap of 2.3 eV,<sup>[10]</sup> long carrier lifetimes, and high collection efficiency.<sup>[14]</sup> Another halide semiconductor of special interest is copper iodide (CuI) because of its high hole mobility (>40 cm<sup>2</sup> (V s)<sup>-1</sup> in bulk).<sup>[7]</sup> CuI exists in different forms: zinc-blende structure below 643 K ( $\gamma$ -CuI), wurtzite structure between 643 and 673 K ( $\beta$ -CuI), and rock salt structure above 673 K ( $\alpha$ -CuI). CuI is a direct bandgap semiconductor, with a bandgap energy of 3.1–3.2 eV, already used in PEC processes.<sup>[12,13,15]</sup> The conduction band (CB) position of both CuI and PbI<sub>2</sub> is suitable for nitrate reduction. By combining these two semiconductors we aimed to cover a broader range of the solar spectrum; therefore, nanocomposites of CuI and PbI<sub>2</sub> with different molar compositions were prepared. There are two major outcomes of this work: first an enhanced PEC performance was demonstrated for the nanocomposites because of cross-excitation from CuI to PbI<sub>2</sub>, along with vertical charge separation. Second, N<sub>2</sub> gas and NO<sub>2</sub><sup>-</sup> were formed through the PEC reduction of NO<sub>3</sub><sup>-</sup>, with high FE and without any H<sub>2</sub> evolution. The mechanism underpinning the improved PEC performance is also discussed in what follows.

## 2. Results and Discussion

### 2.1. Physical Characterization

We first studied the phase diagram of the CuI–PbI<sub>2</sub> nanocomposite.<sup>[16]</sup> Figure 1a shows the phase diagram, together with the optical images of samples of different compositions (the melted mixture is also shown). There is no discernible new bimetallic iodide compound in the system, only a mixture of solid  $\gamma$ -CuI and PbI<sub>2</sub>. Furthermore, at 50 n/n% PbI<sub>2</sub> content the

system has an eutectic point where the melting starts already around 300 °C (as opposed to 606–404 °C of pure materials). As described in Figure S5, Supporting Information, the heating and cooling “path” on the phase diagram during the electrode preparation may influence the homogeneity of the resulting mixture. Based on the phase diagram, the most homogeneous distribution of the CuI–PbI<sub>2</sub> nanocomposite is expected at the eutectic point.

X-ray diffraction (XRD) furnished evidence on the formation of a highly crystalline mixture. Figure 1b shows diffraction patterns of CuI, PbI<sub>2</sub>, and CuI–PbI<sub>2</sub> (50–50%) after melting. Diffraction patterns of CuI and PbI<sub>2</sub> are well aligned with their corresponding International Centre for Diffraction Data (CuI: Card# 26-1150; PbI<sub>2</sub>: Card#: 060246). The unassigned peaks were related to the aluminum sample holder (37.4°, 43.6°, and 64°) and to the FTO substrate (peak at 52.5°) (Figure S6c, Supporting Information). The XRD pattern of mixture of CuI–PbI<sub>2</sub> (50–50%) sample before melting (Figure S6a, Supporting Information) showed all the major peaks of these two parent compounds, but after melting, the diffractions related to plane (111) of CuI and planes (001), (003), and (004) of PbI<sub>2</sub> become dominant (Figure 1b).<sup>[17]</sup> These peaks appeared in the XRD pattern of all nanocomposite samples (containing different molar ratio of CuI and PbI<sub>2</sub>) (Figure S6b, Supporting Information).<sup>[18]</sup> This trend suggests that large, uniform crystal domains are present in the samples. In parallel, the relative intensity of the CuI (220) and (311) diffractions decreased, indicating the recrystallization during the synthesis process (see further discussion in Figure S5, Supporting Information). Notably, no new diffraction peak developed, which would correspond to a new phase, as suggested by precedent literature.<sup>[19,20]</sup>

Electron microscopy images were taken for the CuI, PbI<sub>2</sub>, and CuI–PbI<sub>2</sub> (50–50%) samples before and after heat treatment, to probe their morphological attributes. Both CuI and PbI<sub>2</sub> appeared as few micron-sized particles before heat treatment on the scanning electron microscopy (SEM) images (Figure S7a,b, Supporting Information). No obvious change was seen in the morphology of CuI upon the heat treatment (Figure S7b, Supporting Information) because the melting of

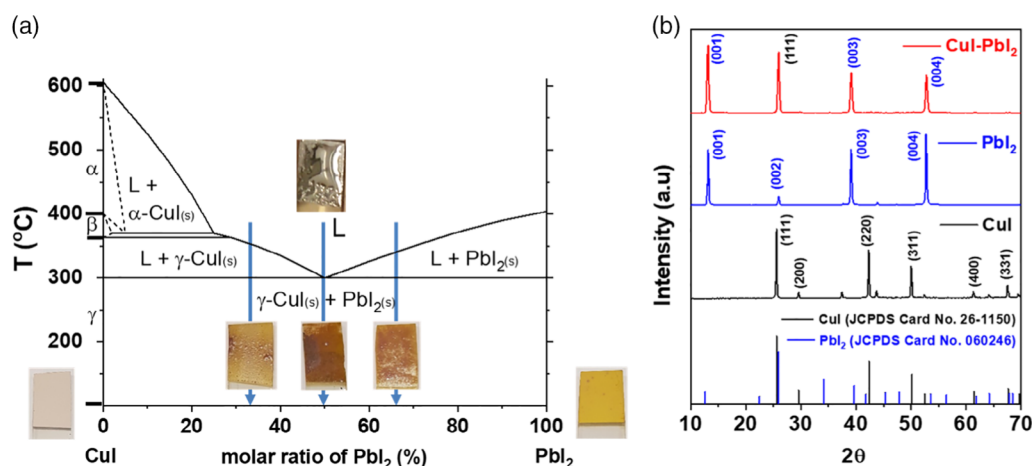


**Figure 1.** a) Phase diagram of the CuI–PbI<sub>2</sub> system adopted from ref. [23] with presentation of three different pathways from the melted thin film to the solid, highly crystalline film. The dark gray molten metal-like liquid illustrates the melted nanocomposite. L stands for liquid. b) XRD pattern of CuI, PbI<sub>2</sub>, and CuI–PbI<sub>2</sub> (50–50%) after heat treatment.

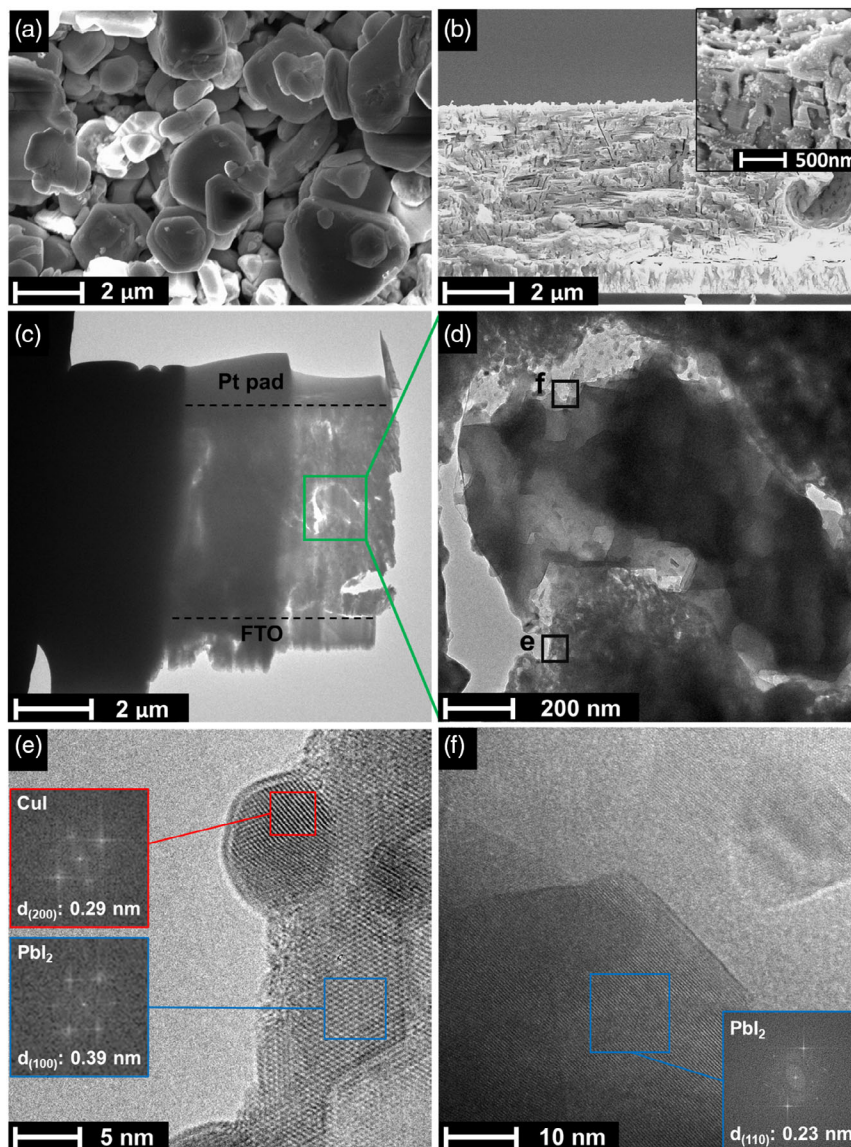


**Figure 2.** a) SEM topographical images of CuI + PbI<sub>2</sub> mixture before heat treatment, and b) cross-sectional view of CuI–PbI<sub>2</sub> (50–50%) after the thin film melting process. Prepared cross-sectional TEM lamellae from melted CuI–PbI<sub>2</sub> (50–50%) at c) lower and d) higher magnification. HR-TEM image from the selected areas in part (d), with e,f) fast Fourier transform (FFT) images from different area as insets.

pure  $\gamma$ -CuI occurs around 606 °C. In the case of pristine PbI<sub>2</sub> however, after the heat treatment the particles melted, and a sheet-like appearance was developed (Figure S7c,d, Supporting Information). In the CuI–PbI<sub>2</sub> (50:50%) mixture, micron-sized particles are visible initially (Figure 2a). Upon heat treatment, however, major changes were spotted. Cross-sectional view demonstrated that a few micrometers thick, semicontinuous film was formed upon the melting process (Figure 2b). In the nanocomposite, the melting point of the components was reduced (see also the phase diagram in Figure 1a), thus both components are melted at 400 °C. In the sheet-like structure, CuI nanoparticles are well dispersed on the highly ordered PbI<sub>2</sub> matrix, as exemplified in Figure 2b. This ordered morphology is retained in long range and provides fertile ground for facile charge carrier extraction as detailed in what follows.

To further visualize this structure, cross-sectional transmission electron microscopy (TEM) lamellae were prepared from the melted CuI–PbI<sub>2</sub> (50–50%) photoelectrode with an SEM–focused ion beam (FIB) instrument (see details in Section 4). The TEM lamellae are shown in Figure 2c, where the Pt pad is seen on the top surface of the photoelectrode (for moving and fixing the lamellae) and the FTO layer, which is connected to the melted CuI–PbI<sub>2</sub> (50–50%) layer. Figure 2d shows a higher magnification image of the ion beam thinned part of the lamellae, where it was transparent for electrons. Two apparently different points were selected from this area, for further imaging (Figure 2e,f). High-resolution TEM (HR-TEM) images confirmed that both components (CuI and PbI<sub>2</sub>) exist in a highly crystalline form (as expected from XRD analysis). Careful fast Fourier transform (FFT) analysis of HR-TEM



images showed that  $\text{PbI}_2$  forms the matrix upon heat treatment and  $\text{CuI}$  particles are distributed either on the surface of  $\text{PbI}_2$  or they can be trapped among the  $\text{PbI}_2$  sheets. Due to the size of the  $\text{CuI}$  particles ( $11 \pm 6$  nm), the resulting composite can be considered as a nanocomposite. It was observed in Figure 2d–f that within the homogeneous  $\text{CuI-PbI}_2$  nanocomposite domains, there  $\text{CuI}$ -free, highly crystalline pure  $\text{PbI}_2$  parts. The formation of these inhomogeneities may be due to the thin film melting technique (see more at Figure S5, Supporting Information).

At this juncture, we refer to Section 4 and related figures (Figure S2a,b, Supporting Information), where we show the color of the electrodes, which also changes upon melting (shifts to orange-reddish color). This predicts that the optical properties of the nanocomposites are different from those of their constituents. Figure 3a shows the optical absorption features of  $\text{CuI}$ ,  $\text{PbI}_2$ , and  $\text{CuI-PbI}_2$  (50–50%). While the spectrum of  $\text{PbI}_2$  showed an absorption onset at 544 nm (translating to a 2.28 eV bandgap obtained by Tauc analysis [see also Figure S8 and Table S3, Supporting Information]),  $\text{CuI}$  had a bandgap of 2.93 eV. These absorption bands appeared in the nanocomposite samples as well (Figure S9, Supporting Information). More interestingly, a new optical feature was observed between 550 and 680 nm for all nanocomposite samples (although at different extents), which translates to a new transition at 1.93–1.99 eV energy values (Figure S8b and S9, Supporting Information). All absorption spectra, together with the determined bandgap energies, can be found in Figure S9 and Table S3, Supporting Information. This feature is indeed interesting, considering that no new compound was formed (based on our XRD and electron diffraction studies). The origin of this new feature is discussed in Section 2.4, where both experimental and theoretical results are analyzed together as a whole.

To better understand the optical features of the nanocomposites, their light emission properties were studied by exciting the samples at 350 nm (an energy which is sufficient to excite both  $\text{CuI}$  and  $\text{PbI}_2$ ).  $\text{CuI}$  showed two prominent luminescence peaks, a blue emission at 415 nm (ascribed to the radiative recombination of excitons) and a red emission closer to 700 nm related to the presence of iodine vacancies (Figure 3b).<sup>[21,22]</sup> The intensity of photoluminescence (PL) peaks of  $\text{CuI}$  is substantially reduced in the mixture even before heat treatment. After the heat

treatment, however, the PL is *completely* suppressed. This suggests that the contact area between the two constituents increased upon the nanocomposite formation, and consequently enhancing the possibility of charge transfer between them. Among all the nanocomposite samples, the film containing 1:1 molar ratio of  $\text{CuI}$  and  $\text{PbI}_2$  shows the lowest PL intensity (Figure S10, Supporting Information).

## 2.2. Photoelectrochemical Studies

PEC studies were carried out in aqueous 0.1 M  $\text{NaNO}_3$  solutions. Linear sweep photovoltammograms (LSVs), recorded for  $\text{CuI}$ ,  $\text{PbI}_2$ , and  $\text{CuI-PbI}_2$  (50–50%), are shown in Figure 4a. The photocurrents are cathodic in polarity for all samples, indicating a p-type semiconductor behavior. The maximum photocurrent was recorded around 0.61 V versus reversible hydrogen electrode (RHE) (see LSV traces for all the samples in Figure S11, Supporting Information). The maximum photocurrent is plotted as a function of composition in Figure 4b, where the current peaks at the 1:1 molar ratio of  $\text{CuI}$  and  $\text{PbI}_2$  ( $1.2 \text{ mA cm}^{-2}$ ). To find the optimal layer thickness of this particular nanocomposite, the loading was varied systematically. The photocurrent increased gradually up to a point ( $7 \text{ mg cm}^{-2}$ ) with the increasing loading, and after reaching the maximum, it slightly decreased (see Figure S4, Supporting Information).

This trend in the current density is in line with incident photon-to-electron conversion efficiency (IPCE) measurements (see Figure 5), where the maximum efficiency was recorded for the equimolar sample ( $\text{CuI-PbI}_2$  [50–50%]). The wavelength-dependent PEC behavior of the photoelectrodes was studied by recording photoaction spectra. The lowest IPCE values were obtained for the  $\text{CuI}$  sample, whereas the  $\text{CuI-PbI}_2$  (50–50%) nanocomposite showed the highest activity (Figure 5a). The onset of the photocurrent matched with the bandgap for both  $\text{PbI}_2$  and  $\text{CuI}$ . The trend in the IPCE values (recorded at 400 nm) as a function of composition (Figure 5c) mirrored that shown for the photocurrent values in Figure 4b. The IPCE value was zero above 550 nm for  $\text{CuI}$  and  $\text{PbI}_2$ , but interestingly, the nanocomposite samples showed a small, yet significant, current response between 575 and 675 nm (Figure 5b). Importantly, the

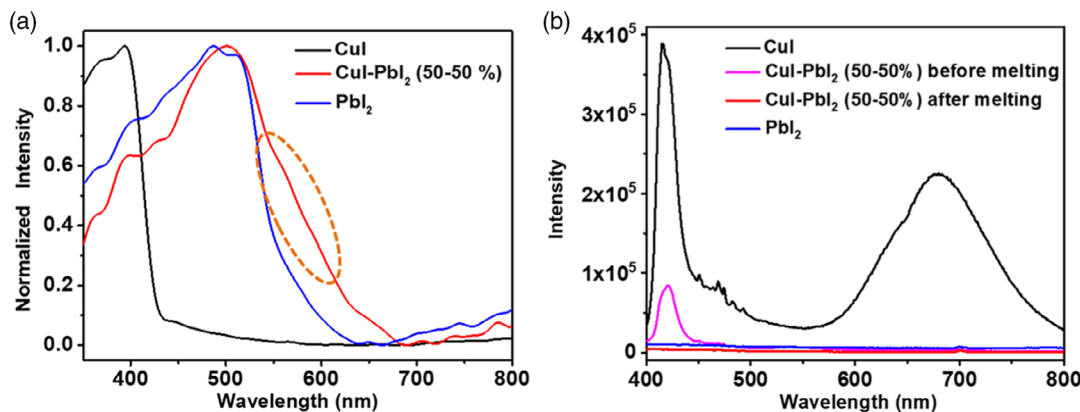


**Figure 3.** a) UV–vis absorption profile of  $\text{CuI}$ ,  $\text{PbI}_2$ , and  $\text{CuI-PbI}_2$  (50–50%) thin films, and b) PL of  $\text{CuI}$ ,  $\text{PbI}_2$ , and  $\text{CuI-PbI}_2$  (50–50%) before and after the heat treatment.

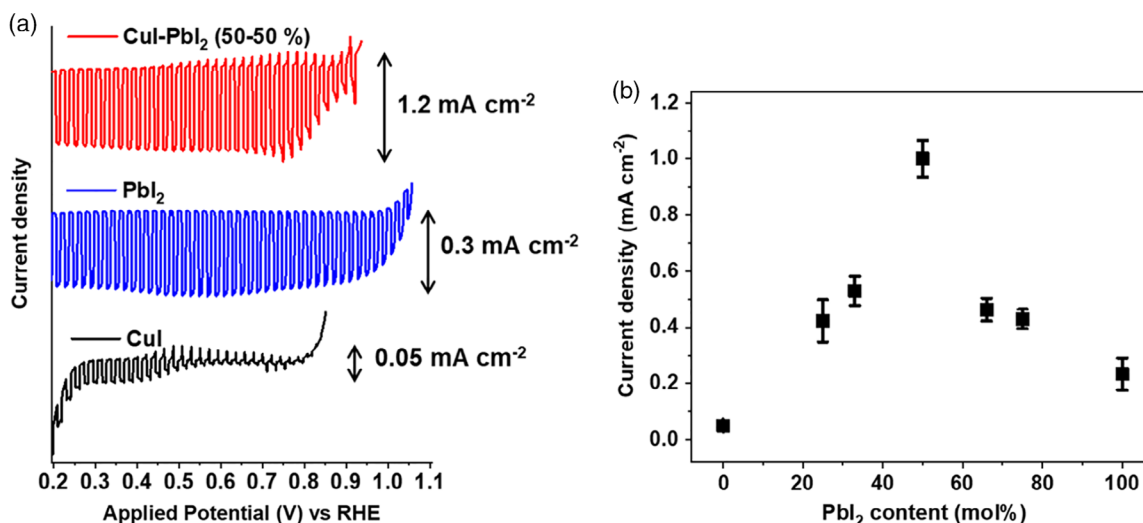


**Figure 4.** LSVs recorded for CuI, PbI<sub>2</sub>, and CuI-PbI<sub>2</sub> (50-50%) in Ar-saturated 0.1 M NaNO<sub>3</sub> solution. a) The sweep rate was kept at 2 mV s<sup>-1</sup>, whereas the light-chopping frequency was 0.2 Hz. b) Maximum current density versus composition of the nanocomposite samples.

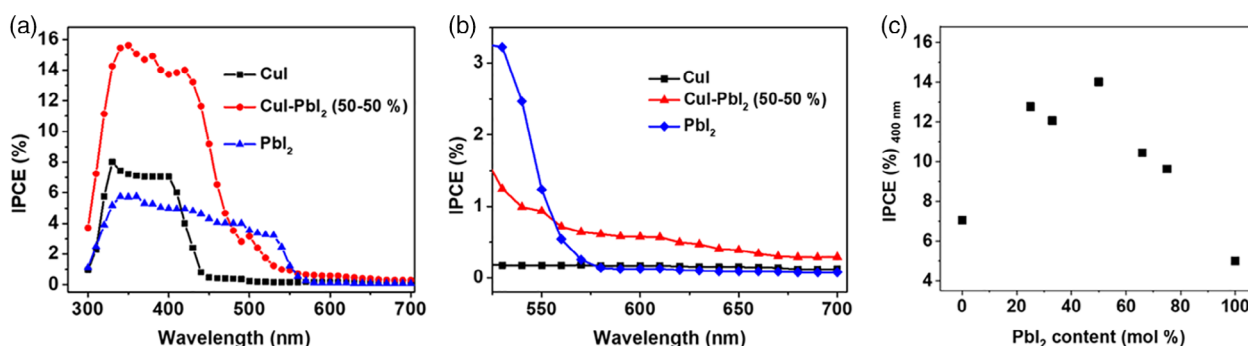


**Figure 5.** a) IPCE curves recorded in 0.1 M NaNO<sub>3</sub> for heat-treated CuI and PbI<sub>2</sub> and CuI-PbI<sub>2</sub> (50-50%) at 0.61 V versus RHE; b) photoresponse of CuI-PbI<sub>2</sub> (50-50%) at wavelength of light between 500 and 700 nm; and c) IPCE values recorded at 400 nm of all the samples.

wavelength range for this new PEC activity matches that of the new absorbance feature, as shown in Figure 3a.

To summarize and put the PEC results into context, it is worth taking another look at the phase diagram shown in Figure 1a. The CuI-PbI<sub>2</sub> (50-50%) sample gave the largest photocurrent density, where the entire film is made of the stoichiometric  $\gamma$ -CuI-PbI<sub>2</sub> nanocomposite phase (without interruption by any crystal of the parent materials). In the cases of other molar ratios, large  $\gamma$ -CuI and PbI<sub>2</sub> crystals are also present in the films and thus break the continuity of the nanocomposite (Figure S5, Supporting Information), explaining the observed volcano curve in Figure 4b. Further discussion on the factors underpinning the enhanced PEC properties is provided in the mechanical insights section.

The stability of the photoelectrodes was investigated by long-term photoelectrolysis at three different potentials (0.46, 0.61, and 0.76 V vs RHE) under periodically interrupted light irradiation (Figure 6 and Figure S12, Supporting Information). A decrease in photocurrent was observed for both CuI-PbI<sub>2</sub> (50-50%) and PbI<sub>2</sub>, although at different extents. PbI<sub>2</sub> corroded and dissolved rapidly, whereas in the nanocomposite this process was much slower and reasonable photocurrents were retained in the course of hours.

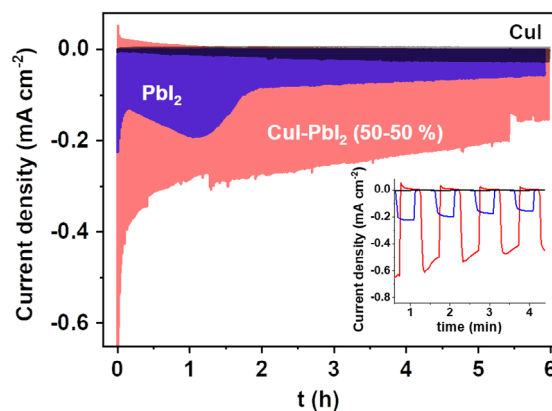


**Figure 6.** Long-term chronoamperometry analysis of heat-treated CuI, PbI<sub>2</sub>, and CuI-PbI<sub>2</sub> (50-50%) photoelectrodes at 0.61 V versus RHE for 6 h in 0.1 M NaNO<sub>3</sub> solution. The inset figure shows chronoamperometric trend of CuI and PbI<sub>2</sub> and CuI-PbI<sub>2</sub> (50-50%) under chopped light irradiation (0.033 Hz) in the first 4 min.

CuI was found to be rather stable, as expected from our precedent results.<sup>[13]</sup> X-ray diffractograms of photocathodes after photoelectrolysis were recorded to understand the chemical changes, and the partial conversion to the respective hydroxides was seen (Figure S13, Supporting Information).

The expected reduction products of nitrate ion are  $\text{NO}_2^-$ ,  $\text{N}_2$ , and  $\text{NH}_3$ , together with  $\text{H}_2$  from the parasite reaction of water splitting reaction. We quantitatively analyzed the amount of nitrite ions using ion chromatography (IC), whereas colorimetric analysis combined with  $^1\text{H-NMR}$  was used for detecting  $\text{NH}_3$ . Gas chromatography coupled mass spectroscopy (GC-MS) studies qualitatively confirmed the formation of  $\text{N}_2$  gas, whereas online GC analysis excluded the formation of  $\text{H}_2$  (see details in the Supporting Information). Aliquots were taken from the electrolyte after 2, 4, and 6 h electrolysis. To accurately quantify the products formed during photoelectrolysis, two control experiments were also carried out: 1) illumination of only the solution in the absence of the electrodes and 2) an experiment under dark with the electrodes in the solution. No product formation was detected in these cases.

The maximum amount of  $\text{NO}_2^-$  was produced at 0.61 V versus RHE, with about 50% FE after 4 h (Figure 7a). The highest  $\text{NO}_2^-$  production rate was  $0.77 \mu\text{mol cm}^{-2} \text{h}^{-1}$  ( $2.14 \times 10^{-10} \text{ mol s}^{-1} \text{ cm}^{-2}$ ), also observed at this potential, and this rate gradually decreased with time (Figure 7b), coinciding with the observed decrease in the photocurrents (Figure 6 and Figure S12, Supporting Information). The error bars on the figure confirm the consistency and reproducibility of  $\text{NO}_2^-$  formation. Notably, all the applied potentials (i.e., 0.46, 0.61, and 0.76 V vs RHE) are over the thermodynamic reduction potential for  $\text{NO}_3^-$  ( $-0.02 \text{ V vs RHE}$ ; see Figure 9a).

Colorimetric measurements showed the presence of ammonia in the taken samples; however, in the case when the nitrate ion source was the Ar-saturated 0.1 M  $^{15}\text{N}$ -labeled (98%)  $\text{Na}^{15}\text{NO}_3$  solution,  $^1\text{H-NMR}$  measurements proved that this ammonia has not come from the reduction of the nitrate ion but come from an external source of contamination.

As another interesting observation, small bubbles were spotted on the surface of the photoelectrodes during

photoelectrolysis. Online GC analysis of the gas phase was performed during the photoelectrolysis and *no*  $\text{H}_2$  formation was seen in any of these experiments. Therefore, we assumed that the formed bubbles are  $\text{N}_2$ . Isotope labeling experiments confirmed this notion, and the underlying data and discussion are shown in Figure S14, Supporting Information. We think that the missing charge density (i.e., to achieve 100% total FE) can be partially accounted to  $\text{N}_2$  formation (apart from the photocorrosion).

### 2.3. Computational Studies

Density functional theory (DFT) was used to investigate the structure and electronic band alignment of the hybrid in a more detailed fashion.  $\text{PbI}_2$  has a rhombohedral crystal structure with space group of  $P3\bar{m}1$  (164). The lattice parameters are  $a = b = 4.56 \text{ \AA}$ ,  $c = 7.00 \text{ \AA}$ ,  $\alpha = \beta = 90^\circ$ , and  $\gamma = 120^\circ$ . As shown in Figure S15a, Supporting Information, in a primitive unit cell, one Pb atom is located at origin and two I atoms are at  $(1/3, 2/3, +z)$  and  $(2/3, 1/3, -z)$ , where  $z$  is  $1.86 \text{ \AA}$ . The space group of zinc-blende CuI ( $\gamma\text{-CuI}$ ) is  $F4\bar{3}m$  (216). In a conventional face center cubic cell, a Cu atom is located at the origin and a I atom at  $(\frac{1}{4}, \frac{1}{4}, \frac{1}{4})$ . Thus, each Cu(I) atom has four nearest neighboring I(Cu) atoms in a tetrahedral configuration (Figure S15, Supporting Information). The direct bandgap of CuI bulk appeared on A point is  $3.00 \text{ eV}$  which is in good agreement with experiment results. The crystal and electronic and structures are schematically represented in Figure S15, Supporting Information.

Subsequently, the  $\text{PbI}_2(001)$  and  $\text{CuI}(111)$  slabs were investigated, as they are the most prominent in the nanocomposite material. The zinc-blende CuI in the direction  $[111]$  consists of a sequence of alternate hexagonal Cu-I bilayers with layer distance of  $3.50 \text{ \AA}$ , as shown in Figure 8a. The  $\text{CuI}(111)$  slab alternately arranged by a layer of Cu cation and a layer of I anion; therefore, it produces permanent dipole moment in the slab. Such a polar surface is not stable in realistic environment. Mostly, electronic reconstruction occurs via surface adsorption or atomic reconstruction by adding or removing surface atoms would neutralize the polar surface. However, the surface

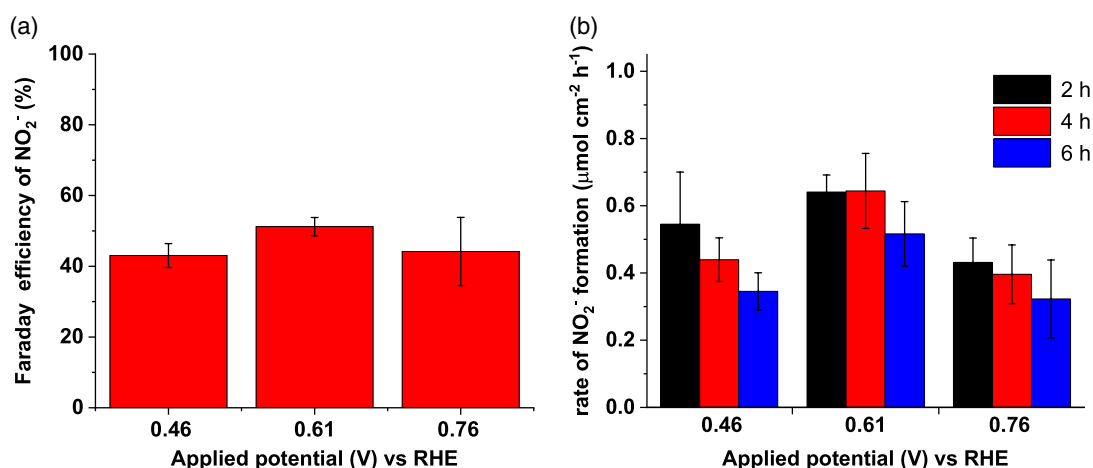


**Figure 7.** a) Faradaic efficiencies of  $\text{NO}_2^-$  ion formation after 4 h during the photoelectrolysis and b) formation rates (the amount of  $\text{NO}_2^-$  ion produced per hour and divided by the geometric area of the photoelectrode) with the irradiation time at constant applied potentials (0.46, 0.61, and 0.76 V vs RHE) on CuI– $\text{PbI}_2$  (50–50%) photoelectrode in 0.1 M  $\text{NaNO}_3$  solution.

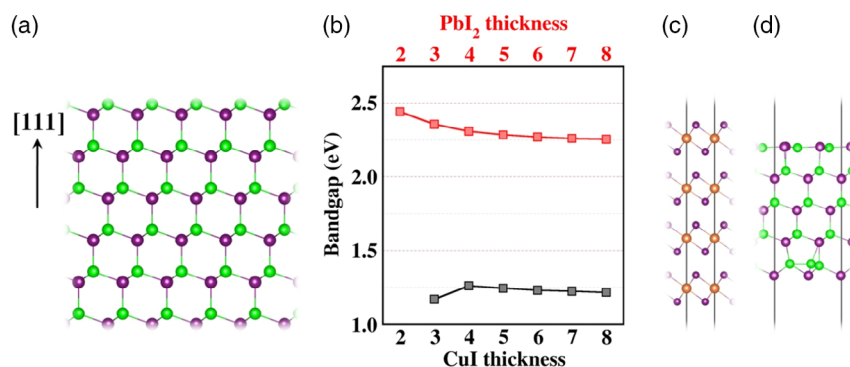


**Figure 8.** a) Schematic of bulk CuI. b) The PBE bandgap of PbI<sub>2</sub> and CuI with different number of layers. c) Schematic of four-layers PbI<sub>2</sub>(001) slab. d) Schematic of five-layers reconstructed CuI(111) slab.

morphology of CuI(111) on PbI<sub>2</sub>(001) is not understood. Scanning tunneling microscopy study of CuBr(111) surface growth on Cu substrate<sup>[23]</sup> indicated a (2 × 2) ordered vacancy structure, resulting in a surface reconstruction that formed by three Br or three Cu atoms with one nearest neighbor missing. This (2 × 2) reconstruction would yield a neutral surface, and it has also been observed for CuBr film on MgO(100)<sup>[24]</sup> and zincblende GaAs(111) surface.<sup>[25]</sup> We therefore consider (2 × 2) reconstruction of CuI(111) slab on both Cu-terminated and I-terminated faces and the result is shown in Figure 8d. In addition, we used Perdew–Burke–Ernzerhof (PBE) functional to evaluate the slab thickness (size) effect of these two slabs and the result is in Figure 8b. As one can see, the PBE bandgaps of eight-layers PbI<sub>2</sub> and CuI slabs are 2.25 and 1.21 eV, respectively. Consequently, we simulate PbI<sub>2</sub>(001) and CuI(111) slabs by using four (see Figure 8c) and five layers, respectively, which are converged.

The band alignment between the PbI<sub>2</sub>(001) and CuI(111) slabs with respect to the vacuum levels was also studied. To accurately align the vacuum levels, we used cutoff energies of 500 eV and *k*-point sampling of 3 × 3 × 1 for both PbI<sub>2</sub>(001)-2 × 2 and reconstructed CuI(111)-2 × 2. The relative band edge alignment perfectly mirrored the experimental data. This result indicates that in the CuI@PbI<sub>2</sub> combined system VB maximum is

contributed from CuI and CBM is contributed from PbI<sub>2</sub>, thus the bandgap is 1.82 eV which is entirely consistent with the experimental observations (see also Figure 9a). More than 50 different interface configurations of CuI@PbI<sub>2</sub> were calculated, but all results show significant changes in electronic structure. It reveals that CuI is plausibly bonding with PbI<sub>2</sub> through weak van der Waals interaction because the resultant interface might give only minor influence.

We extended these DFT studies to understand the inhibition of H<sub>2</sub> production during nitrate reduction. The adsorption energy of H<sub>2</sub> on PbI<sub>2</sub> (001) and CuI (111) was calculated (also taking into account possible surface reconstruction). Both processes possessed very high positive Gibbs free energy values. As PbI<sub>2</sub> (001) and CuI (111) planes are identified in our XRD and TEM analysis as dominant facts, we assume this is a plausible reason for suppressing H<sub>2</sub> generation. Detailed discussion on calculation and related figures (Figure S16–S18, Supporting Information) are included in the SI.

#### 2.4. Mechanistic Insights

XRD and HR-TEM investigations showed that PbI<sub>2</sub> and CuI do not form any new compound upon heat treatment, instead they

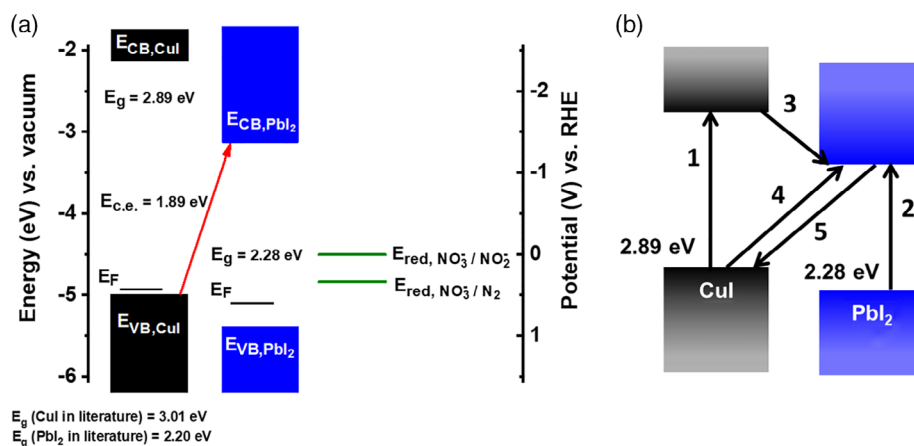


**Figure 9.** a) Band diagram of CuI and PbI<sub>2</sub> the reduction potential for NO<sub>2</sub><sup>-</sup> and N<sub>2</sub> is set versus RHE. b) Various pathways of electron excitation and recombination within and between CuI and PbI<sub>2</sub>.



retain their individual form in the nanocomposite photoelectrodes. Band diagrams were constructed for both CuI and PbI<sub>2</sub>, to better understand the charge carrier transport and transfer processes (Figure 9a). Ambient pressure photoemission spectroscopy (APS) was used to determine the valence band (VB) positions, whereas the bandgap values were furnished by the Tauc analysis and from IPCE studies. The CB positions were determined using the VB position and the bandgap energy. In addition, Kelvin probe microscopy was also used to determine the Fermi-level position.

Experimental (optoelectronic and IPCE studies) and computational results both confirmed that the new absorption band at 600 nm (1.9 eV) corresponds to the transfer of electrons from the VB of CuI to the CB of PbI<sub>2</sub> (see Figure 9a). Furthermore, the PL intensity of CuI is completely quenched in the nanocomposite samples, indicating rapid charge carrier separation. This assumption was proven in the PEC studies, where higher photocurrents were recorded for the hybrid photoelectrodes compared with their single component counterparts. The maximum photocurrent was obtained when the composition is 1:1, indicating efficient charge transfer from CuI to PbI<sub>2</sub> in this case.

Various pathways of electron excitation and recombination are shown in Figure 9b. Pathways 1 and 2 represent the generation of electron-hole pairs within CuI and PbI<sub>2</sub>, respectively. The additional two pathways 3 and 4 are expected to be the reasons behind the improved PEC performance of CuI–PbI<sub>2</sub> nanocomposites. Excited electrons in the CB of CuI can be transferred to the CB of PbI<sub>2</sub> (3). Along with this event, the electrons in the VB of CuI can be excited to the CB of PbI<sub>2</sub> (4), which is responsible for the new absorption feature. These electrons are then available for chemical reactions or may recombine with the holes in CuI or PbI<sub>2</sub> (5). This recombination can decrease the performance of CuI–PbI<sub>2</sub> hybrid photoelectrode. Considering the significant improvement in the photocurrent of hybrid, it can be assumed that pathways 3 and 4 are dominant over 5.

### 3. Conclusions

The possibility of PEC reduction of nitrate to nitrite ion and nitrogen gas without formation of H<sub>2</sub> was demonstrated on CuI–PbI<sub>2</sub> nanocomposite photoelectrodes. IPCE values up to 15% were realized in a broad wavelength range, whereas the maximum FE for NO<sub>2</sub><sup>−</sup> formation was over 52%. While the nanocomposite photocathodes always outperformed the pure CuI and PbI<sub>2</sub> counterparts, the equimolar composition was found to give maximum photocurrent. Detailed optical, PEC, and computational studies gave evidence on the possibility of electron transfer from the VB of CuI to the CB of PbI<sub>2</sub> upon illumination, thus extending the visible light photoactivity of the photoelectrodes. This additional electron excitation, together with the vertical charge carrier separation in the nanocomposite, plays a vital role in improving the performance of hybrid samples. While metal halides are generally considered to be unstable photoelectrodes, in our hands they were by no means inferior compared with their p-type oxide counterparts (note the relative stability during 6 h photoelectrolysis). Furthermore, the fact that the HER was *completely* suppressed projects an interesting future for these nanocomposite metal halide photoelectrodes.

### 4. Experimental Section

**Preparation of CuI and PbI<sub>2</sub>:** We synthesized CuI and PbI<sub>2</sub> by the following methods to obtain a suitable particle size distribution for the suspension preparation. All chemicals used were of analytical grade and were used as received.

**CuI:** 2.0 g of copper acetate was dissolved in 400 mL ultrapure deionized water ( $\rho = 18.2 \text{ M}\Omega \text{ cm}$ ; Millipore Direct Q3-UV); 12–14 mL of 57 wt% hydroiodic acid (HI) was diluted into 200 mL deionized water. The copper acetate solution was added dropwise to the diluted ( $\approx 3.5 \text{ wt}\%$ ) HI solution slowly, under stirring. CuI is formed as pale pink precipitate, which was separated by vacuum filtration and was washed with absolute ethanol until it became white (eliminating iodine contamination). This solid product was dried at 80 °C for 20 min to yield a white powder.

**PbI<sub>2</sub>:** 2.0 g of lead acetate was dissolved in 380 mL deionized water + 20 mL absolute ethanol solution. This solution was added to dilute HI using dropping funnel, and then the bright yellow PbI<sub>2</sub> was separated and dried, similarly as in the case of CuI preparation.

**Preparation of CuI–PbI<sub>2</sub> Nanocomposite Photoelectrode:** Different molar compositions of CuI and PbI<sub>2</sub> were prepared by dispersing both compounds in absolute ethanol by ultrasonic treatment. The total weight of all the composition was kept 0.4 g in 20 mL absolute ethanol (in the case of 1:1 molar ratio it was 0.117 g CuI + 0.283 g PbI<sub>2</sub>). The formed dispersion was spray-coated on cleaned (5–5 min ultrasonication in acetone and ethanol) and preheated fluorine-doped tin oxide-coated glass (FTO) electrodes, using an Alder AD320 type airbrush, with a custom-made fully automated spray coater machine. During the spray-coating process, the electrodes were masked to have a surface area of  $1 \times 1 \text{ cm}^2$  ( $2 \times 1.5 \text{ cm}^2$  for long-term PEC measurements). The loading on the supporting electrodes was quantified by analytical mass balance measurement. Pure PbI<sub>2</sub> and CuI films were also prepared similarly. The mixture was melted on the FTO surface at 400 °C for 5 min under argon gas. Schematic representation of samples preparation is shown in Figure S1, Supporting Information, and the photographs of samples are shown in Figure S2, Supporting Information. The heat treatment parameters and optimal loading mass were the result of preliminary experiments (Figure S3 and S4, Supporting Information).

**Characterization:** The morphology of the samples was studied using TEM, FEI Tecnai G<sup>2</sup> 20 X-Twin, operating at an acceleration voltage of 200 kV. Samples for TEM imaging were prepared by scratching the film from the FTO substrate and dispersing it in ethanol. This suspension was then dropped onto copper grid for analysis. TEM lamellae were also prepared with a Thermo Scientific Scios 2 SEM-FIB instrument. Briefly, to protect the surface a  $12 \times 5 \mu\text{m}^2$  Pt pad was deposited on the surface of the sample with a 2  $\mu\text{m}$  thickness. Two trenches with a depth of 7  $\mu\text{m}$  were cut with ion beam on both sides of the Pt pad. The EasyLift high-precision needle was welded to this Pt pad. With an undercut, a 5  $\mu\text{m}$  deep slice of the sample was removed. This was transferred and attached to a half-moon TEM grid, where it was gradually thinned down and finally polished with the ion beam, to the point where it was transparent for electrons. Cross-sectional images of the nanocomposite layers were taken using SEM, model Hitachi S-4700 coupled with a Röntec EDX detector, operating at an acceleration voltage of 10 kV. X-ray powder diffraction experiments were carried out on a Rigaku SmartLab diffractometer (Cu KR1 radiation  $\lambda = 1.5406 \text{ \AA}$ ). Optical absorption spectra were recorded using Avantes AVASpec-2048 type instrument, equipped with an AvaSphere-30 type integrating sphere. PL of the samples is measured using Jobini Yuou Fluorolog-3 spectrometer and a Horiba Deltaflex spectrometer. IPCE was measured using Newport Quantum Efficiency Measurement System (QEPVSI-B) in a single-compartment, three electrode quartz electrochemical cell, in the wavelength range 300–700 nm ( $\Delta\lambda = 20 \text{ nm}$  step size), at  $E = 0.61 \text{ V}$  (vs RHE), in Ar-saturated 0.1 M NaNO<sub>3</sub> electrolyte.

Kelvin probe microscopy (KP Technology APS04 instrument) was used to measure the Fermi-level position,<sup>[26]</sup> whereas APS was used to detect photoelectrons emitted from VB, and thus determining VB positions.<sup>[27]</sup> Tauc analysis was performed on the optical absorption spectra to obtain the bandgap energy values, which were further confirmed by IPCE data.



The CBCB positions were calculated from the VB positions and the bandgap energy values.

**PEC Measurements:** All PEC measurements were performed on a Metrohm Autolab PGSTAT204 type potentiostat/galvanostat. Three electrode systems were used, where the CuI–PbI<sub>2</sub> nanocomposite on FTO functioned as working electrode, Pt foil as counter electrode, and Ag/AgCl/3M NaCl as reference electrode. The geometrical surface area of the working electrode was 1 cm<sup>2</sup>, except for product detection tests (geometrical surface was 3 cm<sup>2</sup> in this case); 0.1 M NaNO<sub>3</sub> was used as electrolyte. Prior to all measurements, Ar gas was thoroughly purged through the cell for 30 min. LSVs were recorded between +0.38 to –0.4 V versus Ag/AgCl/3M NaCl, as the photoelectrodes were found to be stable in this range. The long-term photoelectrolysis was also carried out at three different potentials (–0.1, +0.05, and +0.2 V vs Ag/AgCl/3 M NaCl) for 6 h, in a two-compartment, sealed electrochemical cell (separated by a Nafion-117 membrane). The potential values were converted to the RHE scale using the following equation:  $E \text{ (RHE)} = E \text{ (Ag/AgCl/3 M NaCl)} + 0.059 \text{ pH} + E^\circ \text{ (Ag/AgCl/3 M NaCl)}$ . LSV traces and long-term photoelectrolysis were recorded under periodically interrupted light irradiation, using a Newport LCS-100 type solar simulator, operated at full output, always placed at a fixed distance of 5 cm from the working electrode (concentrated light, equal to intensity of 6 sun irradiation).

**Product Analysis:** The most likely products of NO<sub>3</sub><sup>–</sup> ion reduction are NO<sub>2</sub><sup>–</sup>, N<sub>2</sub>, and NH<sub>3</sub>. The amount of nitrite formed via nitrate reduction was quantified using IC. All IC measurements were performed with a Dionex DX300 gradient chromatographic system (Dionex, Sunnyvale, CA, USA) that consisted of a CHA-6 high pressure chromatographic module, Dionex EDM eluent degas module and an Advanced Gradient Pump module. Suppressed conductivity detection was used during chromatographic runs. The injection unit (Model 9125, Rheodyne, Rohnert Park, CA, USA) contained 50 µL injection loop. Separations of cations were carried out by a Dionex IonPac CS16 columns (3 × 250 mm). 12.5 mM methanesulfonic acid was used as eluent at 0.5 mL min<sup>–1</sup> flow rate. Anions were separated by a Dionex IonPac AS15 column (2 × 250 mm) using 35 mM KOH eluent at 0.3 mL min<sup>–1</sup> flow rate.

The presence of ammonia in the product was tested by modified Berthelot test (indophenol method).<sup>[28]</sup> Liquid aliquots for the test were taken regularly during photoelectrolysis and the aliquots were tested using colorimetric method. We examined whether the detected ammonia (by the indophenol method) was indeed derived from the reduction of the nitrate ion. For this purpose, an Ar-saturated 0.1 M <sup>15</sup>N-labeled (98%) Na<sup>15</sup>NO<sub>3</sub> solution was used during the photoelectrolysis, where the extent of possible <sup>15</sup>NH<sub>3</sub> formation in the taken aliquots was monitored by <sup>1</sup>H-NMR.

Gas phase products were analyzed with a Shimadzu GC-2010 Plus gas chromatograph equipped with a barrier discharge ionization detector (BID) and a Shincarbon ST column. The cathode compartment of the electrochemical cell was directly connected to the injection unit of the GC with a well-sealed closed loop system, which allowed the online detection of the gas products. For the qualitative detection of nitrogen gas formation, also Ar-saturated 0.1 M <sup>15</sup>N-labeled (98%) Na<sup>15</sup>NO<sub>3</sub> solution was used. During the photoelectrolysis, samples were taken from the gas space and were analyzed by GC-MS. Because the natural occurrence of <sup>15</sup>N<sub>2</sub> gas is low (0.0016%), contamination from the air does not interfere with detecting <sup>15</sup>N<sub>2</sub> produced through the reduction of nitrate ions (see more details in Figure S14, Supporting Information).

**Computational Studies:** The energetics and band alignment of the CuI–PbI<sub>2</sub> nanocomposites were also probed by theoretical means, using DFT, by applying the plane-wave-based code Vienna Ab initio Simulation Package (VASP). The generalized-gradient approximation (GGA) with the PBE functional with the projector augmented wave method<sup>[29]</sup> was adopted. The DFT calculations using PBE functional always underestimate the bandgap energy; therefore, hybrid functional based on Heyd–Scuseria–Ernzerhof (HSE)<sup>[26]</sup> method was introduced to correct the intrinsic bandgap problem.<sup>[30,31]</sup> HSE-type hybrids are semiempirical functionals that incorporate a portion ( $\alpha$ ) of exact exchange from Hartree–Fock theory with exchange correlation from GGA (1– $\alpha$ ). The mixing parameter  $\alpha = 0.25$  was found to be optimal in HSE06 and it can be properly tuned if standard HSE06 underestimates the bandgap.<sup>[30]</sup> In this work, HSE06

functional slightly underestimated the bandgap of both CuI and PbI<sub>2</sub> (Table S2, Supporting Information); therefore, we tuned the mixing parameter  $\alpha$  as 0.35 to reproduce the experimentally obtained bandgaps. The following electronic configurations were assigned to valence electrons of the elements: Pb 6s<sup>2</sup>6p<sup>2</sup>, Cu 3d<sup>10</sup>4s<sup>1</sup>, and I 5s<sup>2</sup>5p<sup>5</sup>. Relativistic effect of spin–orbit coupling (SOC), which is especially important for the heavy element of Pb, was included for all calculations. The long-range van der Waals interactions were taken into account via DFT-D3 correction proposed by Grimme et al.<sup>[32]</sup> In our calculations, convergence of the total energy has been achieved by setting the plane-wave cutoff for the wave function expansion to 500 eV for PbI<sub>2</sub> and 400 eV for CuI. The Monkhorst-Pack<sup>[33]</sup> *k*-point sampling of 6 × 6 × 5 is used for PbI bulk and 7 × 7 × 7 is for CuI bulk. The same configurations are used to calculate H<sub>2</sub> adsorption energy on PbI<sub>2</sub> and CuI.

## Supporting Information

Supporting Information is available from the Wiley Online Library or from the author.

## Acknowledgements

This project has received funding from the European Research Council (ERC) under the European Union's Horizon 2020 research and innovation program (grant agreement no. 716539). This research was partially supported by the “Széchenyi 2020” program in the framework of GINOP-2.3.2-15-2016-00013 “Intelligent materials based on functional surfaces – from syntheses to applications” project. E.K. was supported by the New National Excellence Program of the Ministry for Innovation and Technology (grant no. UNKP-19-3). The authors thank Dr. Krisztián Horváth (University of Pannonia) for advising on ion-chromatography measurements, Mr. Ádám Balog (University of Szeged) for taking SEM images, Dr. Gergely F. Samu for preparing TEM lameallae and for PL measurements, and Dr. Báborka Janáky-Bohner for her help with the manuscript preparation.

## Conflict of Interest

The authors declare no conflict of interest.

## Author Contributions

E.K. and S.T.K. contributed equally to this work. The manuscript was written through contributions of all authors. All authors have given approval to the final version of the manuscript.

## Keywords

CuI–PbI<sub>2</sub> nanocomposites, environmental remediation, nitrate reduction, solar energy conversion, solar fuels

Received: July 27, 2020

Revised: August 26, 2020

Published online:

- [1] S. Jin, *ACS Energy Lett.* **2018**, *3*, 2610.
- [2] R. Saito, H. Ueno, J. Nemoto, Y. Fujii, A. Izuoka, M. Kaneko, *Chem. Commun.* **2009**, *22*, 3231.
- [3] M. Kan, D. Yue, J. Jia, Y. Zhao, *Electrochim. Acta* **2015**, *177*, 366.
- [4] H. Wang, J. A. Turner, *Energy Environ. Sci.* **2013**, *6*, 1802.

- [5] Y. Kim, E. B. Creel, E. R. Corson, B. D. McCloskey, J. J. Urban, R. Kostecki, *Adv. Energy Mater.* **2018**, *8*, 1.
- [6] C. Roy, J. Deschamps, M. H. Martin, E. Bertin, D. Reyer, S. Garbarino, L. Roué, D. Guay, *Appl. Catal. B* **2016**, *187*, 399.
- [7] D. H. Fabini, J. G. Labram, A. J. Lehner, J. S. Bechtel, H. A. Evans, A. Van Der Ven, F. Wudl, M. L. Chabiny, R. Seshadri, *Inorg. Chem.* **2017**, *56*, 11.
- [8] G. F. Samu, R. A. Scheidt, P. V. Kamat, C. Janáky, *Chem. Mater.* **2018**, *30*, 561.
- [9] H. Hsu, L. Ji, M. Du, J. Zhao, E. T. Yu, A. J. Bard, *J. Phys. Chem. C* **2016**, *120*, 2.
- [10] P. A. Beckmann, *Cryst. Res. Technol.* **2010**, *45*, 455.
- [11] K. Lu, Q. Lu, L. Zhang, J. Gong, R. Liu, *J. Electrochem. Soc.* **2017**, *164*, H685.
- [12] T. Baran, S. Wojtyła, A. Dibeneditto, M. Aresta, *ChemSusChem* **2016**, *9*, 1.
- [13] A. Balog, G. F. Samu, P. V. Kamat, C. Janáky, *J. Phys. Chem. Lett.* **2019**, *10*, 259.
- [14] D. Tiwari, D. J. Fermin, *Electrochim. Acta* **2017**, *254*, 223.
- [15] M. Sun, J. Hu, C. Zhai, M. Zhu, J. Pan, *ACS Appl. Mater. Interfaces* **2017**, *9*, 13223.
- [16] T. Takahashi, O. Yamamoto, H. Takahashi, *J. Solid State Chem.* **1977**, *21*, 37.
- [17] B. Sharma, M. K. Rabinal, *J. Alloys Compd.* **2013**, *556*, 198.
- [18] X. H. Zhu, B. J. Zhao, S. F. Zhu, Y. R. Jin, Z. Y. He, J. J. Zhang, Y. Huang, *Cryst. Res. Technol.* **2006**, *41*, 239.
- [19] A. M. Salau, T. A. Kuku, *Solid State Ionics* **1987**, *25*, 1.
- [20] T. A. Kuku, *Thin Solid Films* **1998**, *325*, 246.
- [21] P. Gao, M. Gu, X. L. Liu, B. Liu, S. M. Huang, *Appl. Phys. Lett.* **2009**, *95*, 10.
- [22] N. Yamada, R. Ino, Y. Ninomiya, *Chem. Mater.* **2016**, *28*, 4971.
- [23] C. Y. Nakakura, E. I. Altman, *Surf. Sci.* **1999**, *424*, 244.
- [24] A. Yanase, Y. Segawa, *Surf. Sci.* **1995**, *6028*, 219.
- [25] K. W. Haberern, M. D. Pashley, *Phys. Rev. B* **1990**, *41*, 3226.
- [26] W. Melitz, J. Shen, A. C. Kummel, S. Lee, *Surf. Sci. Rep.* **2011**, *66*, 1.
- [27] I. D. Baikie, A. C. Grain, J. Sutherland, J. Law, *Appl. Surf. Sci.* **2014**, *323*, 45.
- [28] Y. Zhao, R. Shi, X. Bian, C. Zhou, Y. Zhao, S. Zhang, F. Wu, G. I. N. Waterhouse, L. Wu, C. Tung, T. Zhang, *Adv. Sci.* **2019**, *6*, 1802109.
- [29] P. E. Blöchl, *Phys. Rev. B* **1994**, *50*, 17953.
- [30] P. Deák, Q. Duy Ho, F. Seemann, B. Aradi, M. Lorke, T. Frauenheim, *Phys. Rev. B* **2017**, *95*, 1.
- [31] P. Deák, B. Aradi, T. Frauenheim, E. Janzén, A. Gali, *Phys. Rev. B* **2010**, *81*, 1.
- [32] S. Grimme, J. Antony, S. Ehrlich, H. Krieg, *J. Chem. Phys.* **2010**, *132*, 154104.
- [33] H. J. Monkhorst, J. D. Pack, *Phys. Rev. B* **1976**, *13*, 5188.